
OPTIMAL DESIGN OF PHOTONIC NANOJETS UNDER UNCERTAINTY

A PREPRINT

Amal Mohammed A Alghamdi

Department of Applied Mathematics and Computer Science
Technical University of Denmark
DK-2800 Kgs. Lyngby, Denmark

Peng Chen

School of Computational Science and Engineering
Georgia Institute of Technology
Atlanta, GA 30308, USA

Mirza Karamehmedović

Department of Applied Mathematics and Computer Science
Technical University of Denmark
DK-2800 Kgs. Lyngby, Denmark

September 7, 2022

ABSTRACT

Photonic nanojets (PNJs) have promising applications as optical probes in super-resolution optical microscopy, Raman microscopy, as well as fluorescence microscopy. In this work, we consider optimal design of PNJs using a heterogeneous lens refractive index with a fixed lens geometry and uniform plane wave illumination. In particular, we consider the presence of manufacturing error of heterogeneous lens, and propose a computational framework of Optimization Under Uncertainty (OUU) for robust optimal design of PNJ. We formulate a risk-averse stochastic optimization problem with the objective to minimize both the mean and the variance of a target function, which is constrained by the Helmholtz equation that governs the 2D transverse electric (2D TE) electromagnetic field in a neighborhood of the lens. The design variable is taken as a spatially-varying field variable, where we use a finite element method for its discretization, impose a total variation penalty to promote its sparsity, and employ an adjoint-based BFGS method to solve the resulting high-dimensional optimization problem. We demonstrate that our proposed OUU computational framework can achieve more robust optimal design than a deterministic optimization scheme to significantly mitigate the impact of manufacturing uncertainty.

1 Introduction

Photonic nanojets (PNJs) are highly focused beams of light that can arise, e.g., when a laser illuminates a micrometer-sized glass lens. Illuminating a nano-sample with a PNJ produces a far field that is hyper-sensitive to the presence, the properties, and the position of the sample relative to the PNJ. For example Chen et al. [2004], Li et al. [2005], placing a 3D gold nanoparticle sized 2-60 nm inside a PNJ introduces a perturbation in the backscattered far-field intensity anywhere from -35 dB to 15 dB relative to the backscattering intensity of the PNJ-producing micro-lens alone. This and other effects, like the resonant interaction of PNJs with dielectric and plasmonic nanostructures in the sample, make PNJ illumination a promising prospect for simple and inexpensive superresolution optical detection, localization, measurement, imaging, and manipulation Darafsheh [2021], Karamehmedović et al. [2022a].

There are many numerical and a few experimental works attempting PNJ design by structured illumination or by lens shaping Lecler et al. [2019], Zhu and Goddard [2016], Paganini et al. [2015]. Lens shaping optimizes the geometry of a homogeneous lens Chen et al. [2021a], Hengyu et al. [2015] for a fixed illumination and may employ additional structures such as planar supporting substrates, planar substrates with gaps, and combinations of two or more lenses. Some lens shaping studies have allowed limited heterogeneity in the lens refractive index (e.g. layered spheres) Geints et al. [2011]. So far, point-, line-, hollow-focus and multiple-foci PNJ were obtained by structured illumination of

dielectric microspheres, and PNJ position was designed by illuminating micro-scale dielectric spheres, hemispheres and spherical caps, dielectric elliptical particles, cylinders/disks, cuboids, core-shell spheres, core-shell cylinders and core-shell cuboids, spiral axicons, chains of metal-dielectric spheres, chains of core-shell cylinders and low-dimensional parameterized dielectric particles. Recently, Karamehmedović et al. [2022b] studied dynamic PNJ steering using computed structured illumination and a fixed simple homogeneous lens, while Karamehmedović et al. [2022a] applied this steerable optical probe in a numerical demonstration of lateral and vertical super-resolution optical imaging.

The PNJ design scheme we propose and study here involves a fixed-geometry heterogeneous micro-lens. Since a given desired PNJ position requires a specific and detailed optimized lens refractive index profile, it is interesting to perform uncertainty quantification of the PNJ design scheme given lens manufacturing errors and illumination imprecision. Quantifying and mitigating these uncertainties is essential to produce robust optical systems. Nevertheless, there is limited attention in the literature to the effect of these uncertainties and taking them into account in the optimization process.

Our goal with this work is twofold. First, we devise and demonstrate numerically a systematic approach to design PNJ properties, in particular, the PNJ location and intensity. We achieve this by optimizing the heterogeneous lens profile for fixed lens geometry and fixed uniform plane wave illumination. The lens heterogeneity provides flexibility in the PNJ design, as it increases the number of degrees of freedom (DOFs) in the optimal solution. This flexibility eliminates the need for using complex lens shapes and enables achieving the design using, e.g., cylindrical and spherical lenses. Next, we quantify and mitigate the effect of possible manufacturing error using an Optimization Under Uncertainty (OUU) framework. The numerical feasibility of our approach is realized using scalable high-dimensional optimization techniques for PDE-based problems.

We do not expect our computed lens profiles to be experimentally realizable at the moment. Rather, our work is a numerical analysis of the effects of manufacturing and illumination uncertainties on the performance of the proposed PNJ design. In the microwave regime, however, with wavelengths of the order of 1 cm, we do expect the lens profiles to be feasible to produce.

Fig. 1 shows a conceptual illustration of the sample average approximation (SAA)-based OUU framework that we build in section 2. The framework needs as inputs a representation of the manufacturing noise and a design objective, Fig. 1 (top). The latter is normally written in terms of expected values of some stochastic objective and a regularization term. The optimization process starts with an initial design, Fig. 1, (bottom left) at which the objective and its gradient with respect to the design parameters are computed. The gradient is used to create a BFGS step to update the initial design. The framework terminates if the updated design achieves the convergence criteria, otherwise it will continue to create the next BFGS step and repeat the process.

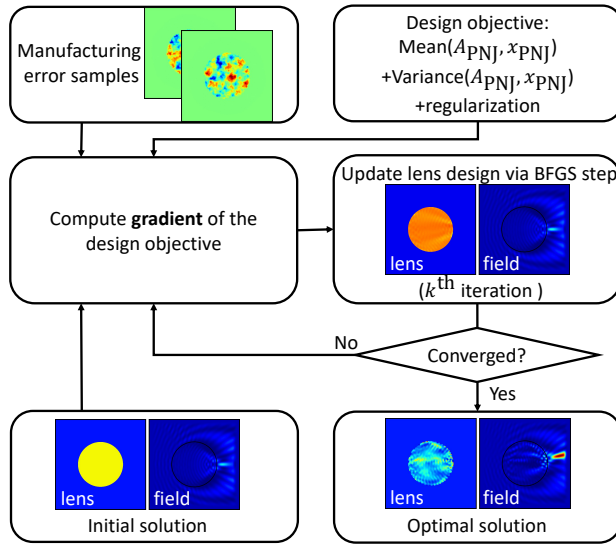


Figure 1: Conceptual illustration of the optimization under uncertainty (OUU) framework. x_{PNJ} and A_{PNJ} are the desired PNJ location and amplitude, respectively.

2 Lens optimization and PNJ design.

2.1 PNJ Model

Fig. 2 illustrates the finite element method (FEM) setup of our direct scattering problem. We consider the light-lens interaction in the time-harmonic 2D transverse electric (2DTE) case with the time-dependence factor $\exp(-i\omega t)$ suppressed. Thus the electric field vector always points outside the plane and may be represented by a complex scalar field u . Let λ_0 and $k_0 = 2\pi/\lambda_0$ be the operating free-space wavelength and wavenumber, respectively. When the lens is illuminated by the \hat{x} -directed, normalized uniform plane wave $u^{\text{inc}}(x, y) = \exp(ik_0 x)$, the produced scattered field u^{sca} satisfies the Helmholtz system

$$\Delta u^{\text{sca}} + k(x, y)^2 u^{\text{sca}} = k_0^2 (1 - n(x, y)^2) \exp(ik_0 x) \quad \text{in } \mathbf{R}^2, \quad (1)$$

$$\lim_{r \rightarrow \infty} r^{\frac{1}{2}} \left(\frac{\partial u^{\text{sca}}}{\partial r} - ik_0 u^{\text{sca}} \right) = 0$$

uniformly in all directions $\frac{(x, y)}{r}$, (2)

where $r = \sqrt{x^2 + y^2}$, $n(x, y) \geq 1$ is the heterogeneous lens refractive index profile for $(x, y) \in \mathcal{D}$, and $n(x, y) = 1$ outside the lens. Finally, (2) is the Sommerfeld radiation condition (approximately modeled by a perfectly matched layer, PML, Turkel and Yefet [1998]).

When referring to a PNJ we shall mean a feature of the total resulting field $u^{\text{tot}} = u^{\text{inc}} + u^{\text{sca}}$ near the lens.

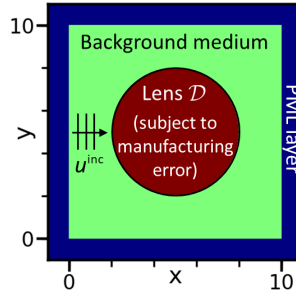


Figure 2: The setup of the forward scattering problem.

2.2 Deterministic Design Problem Formulation

To obtain the desired PNJ, we choose a design objective that maximizes the total wave amplitude at a desired PNJ location, $x_{\text{PNJ}} \in \mathbf{R}^2$. The objective function \mathcal{Q} is given by

$$\mathcal{Q}(u^{\text{tot}}(\tau)) = \frac{1}{2} \int_{\mathbf{R}^2} \delta_{x_{\text{PNJ}}}(x) (|\Re u^{\text{tot}}(\tau)|^2 + |\Im u^{\text{tot}}(\tau)|^2 - A_{\text{PNJ}}^2)^2, \quad (3)$$

where $\Re u^{\text{tot}}$ and $\Im u^{\text{tot}}$ are the real and imaginary parts of the total wave, respectively. We parameterize the wave number as $k = k_0 + e^\tau \chi_{\mathcal{D}}$, where τ is the design variable and $\chi_{\mathcal{D}}$ is a characteristic function with support on the lens \mathcal{D} . $\delta_{x_{\text{PNJ}}}(x)$ is the Dirac delta at x_{PNJ} . A_{PNJ} is the desired PNJ amplitude which we normally set to an unattainable high value to achieve the maximum possible amplitude in practise.

2.3 Stochastic Design Problem Formulation

In optical systems, a stochastic manufacturing error might be present, in the lens properties for example. Here, we assume a lens manufacturing error ζ that we represent as a Gaussian random field with Matérn covariance. The stochastic design objective \mathcal{Q} is now given by

$$\mathcal{Q}(u^{\text{tot}}(\tau, \zeta)) = \frac{1}{2} \int_{\mathbf{R}^2} \delta_{x_{\text{PNJ}}}(x) (|\Re u^{\text{tot}}(\tau, \zeta)|^2 + |\Im u^{\text{tot}}(\tau, \zeta)|^2 - A_{\text{PNJ}}^2)^2, \quad (4)$$

where we update the parameterization of the wave number k to take into account the manufacturing error ζ , $k = k_0 + e^{\tau+\zeta}\chi_{\mathcal{D}}$.

We assume $\zeta \sim \mathcal{N}(0, \mathcal{C})$, where \mathcal{N} , is a zero-mean normal distribution and \mathcal{C} is Matérn-class covariance operator. A scalable approach to obtain samples from the distribution $\mathcal{N}(0, \mathcal{C})$ is to employ the link between Matérn-class Gaussian random fields and elliptic Stochastic Partial Differential Equations (SPDE) Lindgren et al. [2010], see the appendix. In this approach, the covariance operator $\mathcal{C}(\delta, \gamma, \alpha)$ is parameterized by the scalar parameters δ , γ and α that collectively control the variance, smoothness, and correlation length of the field. Fig. 3 shows samples of the described Gaussian random field for $\alpha = 2$, $\gamma = 2.5$, and $\delta = 25$.

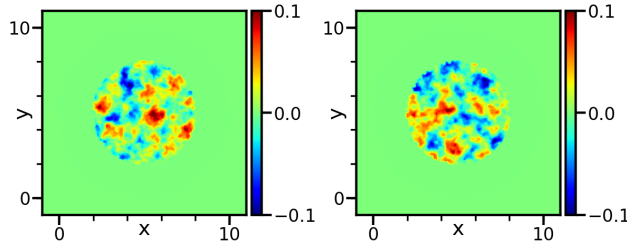


Figure 3: Two samples of the manufacturing error $\zeta \sim \mathcal{N}(0, \mathcal{C})$.

2.4 Optimization under Manufacturing Uncertainty

To formulate the design objective (4) as an OUU problem, we use the risk-averse mean-variance formulation:

$$\mathcal{J}(\tau) = \mathbb{E}_{\zeta}[\mathcal{Q}(\tau, \zeta)] + \beta_V \text{Var}_{\zeta}[\mathcal{Q}(\tau, \zeta)] + \beta_P P(\tau), \quad (5)$$

with the goal to maximize the expectation of the total wave amplitude while minimizing its variability, where \mathbb{E}_{ζ} and Var_{ζ} denotes expected value and variance with respect to the manufacturing error ζ , respectively. β_V is a weight for the variance term. The last term in (5) is a penalty (regularization) term, where $P(\tau) = \int_{\mathcal{D}} |\tau(x)| dx \approx \int_{\mathcal{D}} (\tau^2(x) + \epsilon)^{\frac{1}{2}} dx$ is an approximate total variation penalty function that promotes sparsity of the material and β_P is the penalty term weight. We tune β_V and β_P in practise to control the degree to which we enforce the corresponding terms.

2.5 Numerical Methods

To evaluate the cost functional (5) numerically, we use sample average approximation (SAA) where the mean and the variance in (5) are approximated as follows

$$\mathbb{E}_{\zeta}[\mathcal{Q}(\tau, \zeta)] \approx \bar{\mathcal{Q}} := \frac{1}{M} \sum_{m=1}^M \mathcal{Q}(\tau, \zeta_m), \quad (6)$$

$$\begin{aligned} \text{Var}_{\zeta}[\mathcal{Q}(\tau, \zeta)] &= \mathbb{E}_{\zeta}[\mathcal{Q}^2(\tau, \zeta)] - \mathbb{E}_{\zeta}[\mathcal{Q}(\tau, \zeta)]^2 \\ &\approx \frac{1}{M} \sum_{m=1}^M \mathcal{Q}^2(\tau, \zeta_m) - \bar{\mathcal{Q}}^2, \end{aligned} \quad (7)$$

where M is the number of samples used in the SAA.

In the objective (4), we assume that the solution of the Helmholtz equation (1)–(2), the scattered field u^{sca} , is independent from the design variable τ . We enforce the dependency of the scattered field on τ via constraining the optimization problem with the weak form of the system (1)–(2), details of formulating the weak form for the Helmholtz equation can be found in Chen et al. [2021b]. We denote the weak form of (1)–(2) by

$$a(u_m^{\text{sca}}, v_m; \tau, \zeta_m) = b(v_m) \quad \forall \text{ test function } v_m, \quad (8)$$

where a and b are the bilinear and linear forms of the weak formulation, respectively. We solve the system (8) numerically using finite elements methods.

Finally, we form the Lagrangian objective by adding the constraints (8), for $m = 1, \dots, M$, to the SAA of (5). The Lagrangian is then given as

$$\begin{aligned} \mathcal{L}(\tau) = & \frac{1}{M} \sum_{m=1}^M \mathcal{Q}(\tau, \zeta_m) \\ & + \beta_V \frac{1}{M} \sum_{m=1}^M \mathcal{Q}^2(\tau, \zeta_m) - \bar{Q}^2 \\ & + \beta_P P(\tau) \\ & + \sum_{m=1}^M (a(u_m^{\text{sca}}, v_m; \tau, \zeta_m) - b(v_m)). \end{aligned} \quad (9)$$

The test functions v_m play the role of the Lagrange multipliers in the Lagrangian (9).

We solve the optimization problem of minimizing \mathcal{L} , upon discretization, using BFGS method. To compute the gradient required for BFGS, we form an adjoint-based gradient Gunzburger [2002] which require M forward problem, (8), solves and M corresponding adjoint problem solves. Computing the adjoint-based gradient is scalable since the number of PDE solves required, $2M$, is independent of the number of DOFs of the discretization of τ . We use the python library Stochastic Optimization under high-dimensional Uncertainty in Python (SOUPy) for the SAA based optimization Chen [2021].

3 Numerical results

We present deterministic PNJ design results in sections 3.1 and 3.2. In section 3.3, we study the effect of the manufacturing error through forward uncertainty quantification. In section 3.4, we present application of SAA OUU to the PNJ design problem.

3.1 Optimal lens design

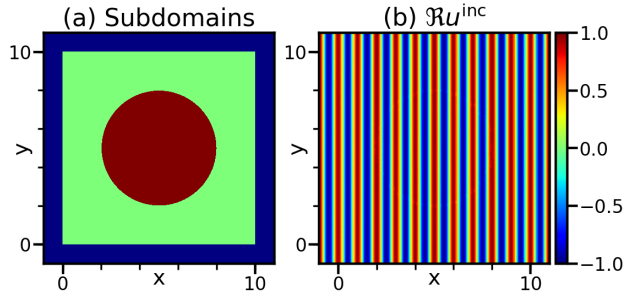


Figure 4: (a) Simulation subdomains: the lens \mathcal{D} (dark red), the background medium (green), and the PML layer (dark blue). (b) The real part of the incident wave u^{inc} .

For all the numerical experiments in this paper, we assume a circular lens of radius 3 units. We set the simulation domain to be of 10 by 10 units and the PML layer width to be 1 unit, Fig. 4a. The incident wave in our simulation is a plane wave given by $u^{\text{inc}}(\mathbf{x}) = \exp(ik_0\mathbf{x}\cdot\hat{\mathbf{b}})$. The real part of u^{inc} is shown in Fig. 4b.

For the initial homogeneous lens profile, Fig. 5a, the resulting total amplitude profile squared is shown in Fig. 5b. We note a PNJ-like formation with maximum amplitude square of about 8 units. Starting from this initial lens profile, we solve the optimization problem of minimizing the deterministic form of the objective (9) ($M = 1$ and $\zeta_m = 0$) where $x_{\text{PNJ}} = (8.5, 5)$ and $A_{\text{PNJ}} = 20$. The solution, the optimal profile, is shown in Fig. 6a. The achieved total amplitude squared field that corresponds to the optimal profile is shown in Fig. 6b. We observe that a PNJ-like formation in the desired location x_{PNJ} is evident and that the maximum amplitude square at the peak of the PNJ formation is significantly larger than the initial amplitude, ~ 22 units. The full width half maximum (FWHM) of the formed PNJ is about 0.54λ , Fig. 6c.

Reduction of the cost and the gradient of the optimization objective using BFGS method Byrd et al. [1995] is shown in Fig. 6b. At around iteration 30, both the cost functional and the gradient norm plateau around constant values as shown

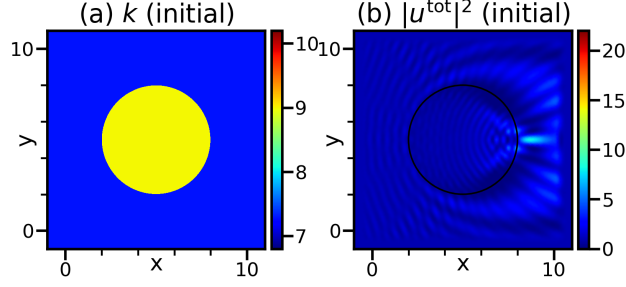


Figure 5: (a) Initial homogeneous lens profile. (b) The total amplitude profile squared that corresponds to the initial lens profile in (a).

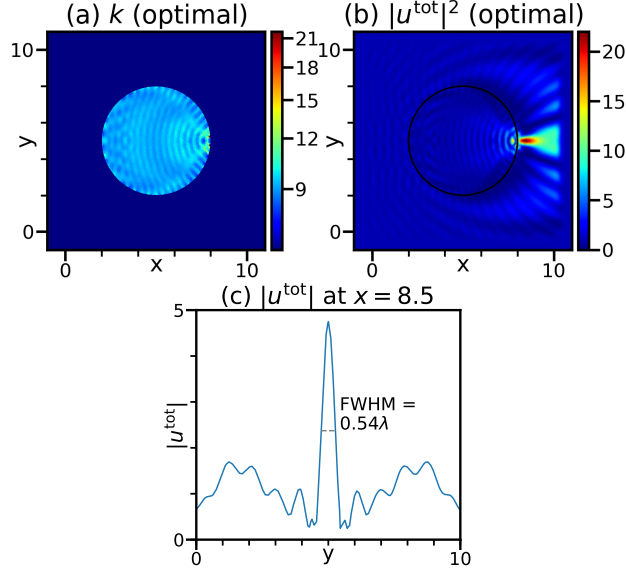


Figure 6: (a) Optimal heterogeneous lens profile and (b) the corresponding total amplitude squared for the case in which $x_{\text{PNJ}} = (8.5, 5)$ and $A_{\text{PNJ}} = 20$. (c) A slice of total amplitude profile at $x = 8.5$ (blue line). The extent of the full width half maximum (FWHM) is marked in a dashed black line.

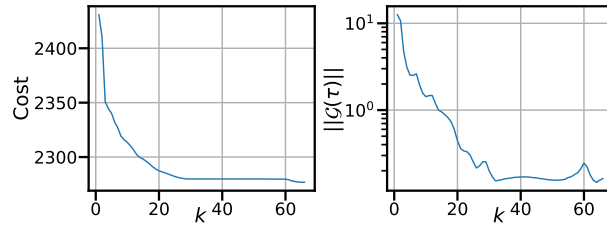


Figure 7: Convergence of BFGS method to the optimal solution in Fig. 6. (left) Cost value versus iteration number. (right) Gradient norm versus iteration number.

in Fig. 7. The optimization is terminated after reaching a maximum backtracking limit of 70. The gradient is reduced, significantly, approximately two orders of magnitude. The cost functional is still relatively large after termination because attaining the desired amplitude of $A_{\text{PNJ}} = 20$ is not possible for the model that we specify, hence the large discrepancy between A_{PNJ} and the achieved amplitude ~ 5 .

3.2 Radial and Angular shift in PNJ location

In this section we present two numerical experiments. In the first one, the desired location is shifted along the radius, $x_{\text{PNJ}} = (9.5, 5)$ and $A_{\text{PNJ}} = 20$. We obtain an optimal lens design, Fig. 8a, that is considerably different from the one we obtain in Fig. 6 and achieves the desired radial shift in the PNJ location. We obtain a PNJ that peaks at $x_{\text{PNJ}} = (9.5, 5)$, Fig. 8b.

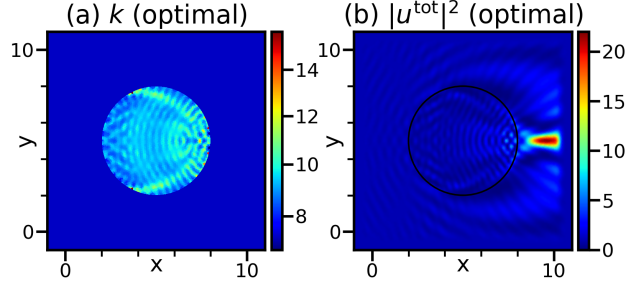


Figure 8: PNJ design with a radial shift in the desired PNJ location. (a) Optimal heterogeneous lens profile and (b) the corresponding total amplitude squared for the case in which $x_{\text{PNJ}} = (9.5, 5)$ and $A_{\text{PNJ}} = 20$.

In the second numerical experiment, the desired location is shifted along the angular direction, $x_{\text{PNJ}} = (8.5, 6)$ and $A_{\text{PNJ}} = 20$. In this case, the optimal lens design that we obtain, Fig. 9a, is non-symmetric and distinct from the previous lens designs. It effectively “bends” the light to achieve the desired PNJ that peaks at $x_{\text{PNJ}} = (8.5, 6)$, Fig. 9b.

Note that the desired PNJ amplitude in the two scenarios we discuss here is ~ 5 while $A_{\text{PNJ}} = 20$. To illustrate the effect of choosing the value of A_{PNJ} , we present a scenario in which $5 < A_{\text{PNJ}} < 20$. We choose $A_{\text{PNJ}} = 7$ and keep $x_{\text{PNJ}} = (8.5, 6)$ unchanged. The optimization in this case fails to produce the PNJ phenomena and the intense light energy is scattered among multiple formations, Fig. 9c and 9d.

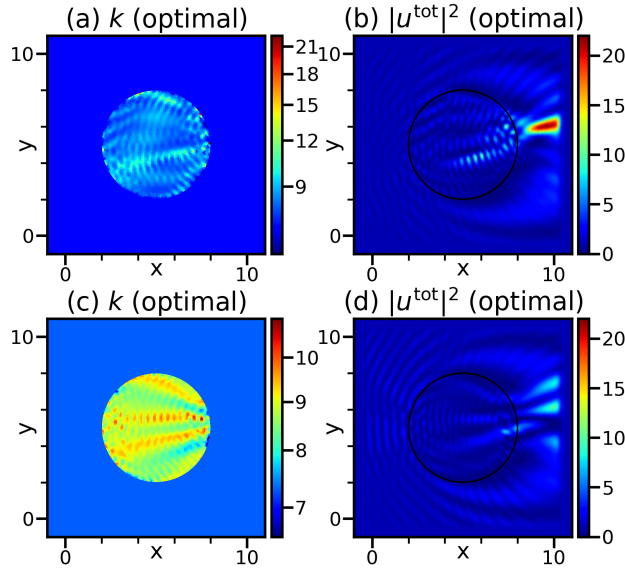


Figure 9: PNJ design with an angular shift in the desired PNJ location. (a) Optimal heterogeneous lens profile and (b) the corresponding total amplitude squared for the case in which $x_{\text{PNJ}} = (8.5, 6)$ and $A_{\text{PNJ}} = 20$. (c) Optimal heterogeneous lens profile and (d) the corresponding total amplitude squared for the case in which $x_{\text{PNJ}} = (8.5, 6)$ and $A_{\text{PNJ}} = 7$.

3.3 Effect of manufacturing noise on PNJ location and intensity

By applying forward uncertainty quantification, we study the effect of manufacturing errors in the lens design on the formed PNJ. We add manufacturing error realizations, obtained from the same distribution from which the realizations

in Fig. 3 are obtained, to the optimal lens in Fig. 9a and solve the forward problem (1) to obtain the corresponding total amplitude squared. We repeat this process for $M = 15$ error realizations. In Fig. 10, we show two cases of the 15 cases. The location and intensity of the result PNJ varies based on the noise realization, e.g. the PNJ in Fig. 10b is slightly different than the one in Fig. 10d. This shows that the presence of manufacturing noise of this magnitude affect the properties of the desired PNJ.

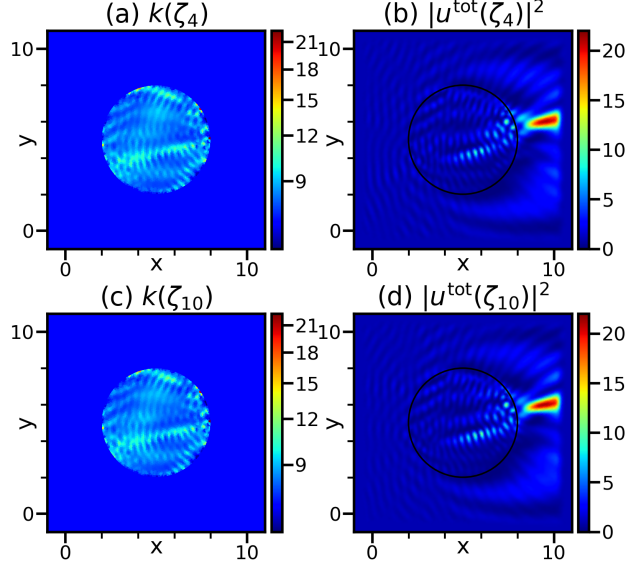


Figure 10: Effect of manufacturing errors on the result PNJ. (a) and (c) Two realizations of the optimal heterogeneous lens profile, Fig. 9a, polluted by two different realizations of the manufacturing noise. (b) and (d) The corresponding total amplitude squared. $x_{\text{PNJ}} = (8.5, 6)$ and $A_{\text{PNJ}} = 20$.

To summarize the variation of PNJ properties due to the $M = 15$ error realizations, we plot a histogram of the PNJ maximum intensity location and maximum amplitude squared, Fig. 11. We note that the maximum amplitude is attained at five different locations with varying statistical frequency, Fig. 11a. These locations are discrete because they correspond to finite element mesh vertices. The maximum total amplitude squared also varies. It attains values ranging from ~ 20.4 to ~ 21.5 , Fig. 11b.

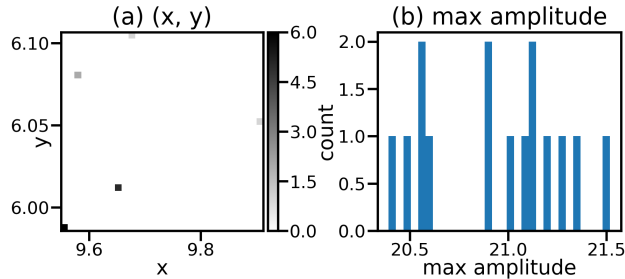


Figure 11: Histogram of the PNJ features resulting from 15 lens profiles. Each of those profiles is the deterministic-based optimal lens, Fig. 9a, polluted by a different manufacturing error realization. (a) PNJ location histogram. (b) PNJ maximum amplitude squared histogram.

3.4 Designing the PNJ under uncertainty

Here we solve the problem of finding the optimal lens design while taking the manufacturing errors into account via using the SAA based OUU formulation as described in sections 2.4 and 2.5. We obtain an optimal lens profile, Fig. 12a, that has visibly different features from the lens profile obtained in the corresponding deterministic setup, Fig. 9. The PNJ formation in the desired location, $x_{\text{PNJ}} = (8.5, 6)$, is evident in the corresponding total amplitude squared profile, Fig. 12b. In this experiment, $M = 15$ and $A_{\text{PNJ}} = 20$.

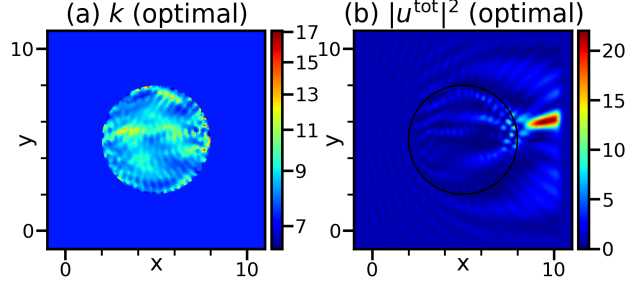


Figure 12: PNJ design under manufacturing uncertainty. (a) The optimal heterogeneous lens profile as a result of minimizing (9). (b) The corresponding total amplitude squared. $x_{\text{PNJ}} = (8.5, 6)$ and $A_{\text{PNJ}} = 20$.

Analogous to the deterministic case, we summarize the PNJ properties for this SAA OUU case in histograms, Fig. 13, to study the effect of the same 15 manufacturing error realizations on the produced PNJ. We see that using SAA OUU approach leads to more robust PNJ properties at the presence of manufacturing errors: For the 15 error samples, the attained PNJ locations are realized in only two points in space (compared to five points in Fig. 11a) and the attained maximum amplitudes are generally higher than those in the deterministic case (Fig. 11b).

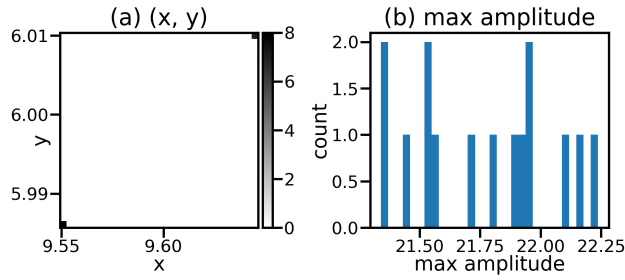


Figure 13: Histogram of the PNJ features resulting from 15 lens profiles. Each of those profiles is the SAA-based optimal lens, Fig. 12a, polluted by a different manufacturing error realization. (a) PNJ location histogram. (b) PNJ maximum amplitude squared histogram.

In table 1a, we provide the mean and the variance for each of the three quantities, the x and y coordinates of the PNJ peak and the total amplitude square value at the peak, for both the deterministic and the SAA OUU cases. In the SAA OUU case, the variance of the PNJ location is notably smaller and the mean of the maximum amplitude is larger when compared to the deterministic case. In table 1b, we show the same quantities for a slightly different numerical experiment in which the noise amplitude is doubled. The results in this case are an evident confirmation of the advantage of using the SAA OUU formulation. The variances of the three quantities are reduced when using SAA OUU compared to the deterministic optimization, and the mean of the attained maximum amplitude is larger.

In Fig. 14, we compare the convergence results of the deterministic and the SAA runs. Overall, the convergence patterns are similar for the two cases. However, if we take a look at the gradient norm plot, Fig. 14 (right), we can see that the convergence of the SAA run is slightly slower compared to the deterministic run. This is expected because of the complicated SAA objective function that has M cost functions to be minimized simultaneously.

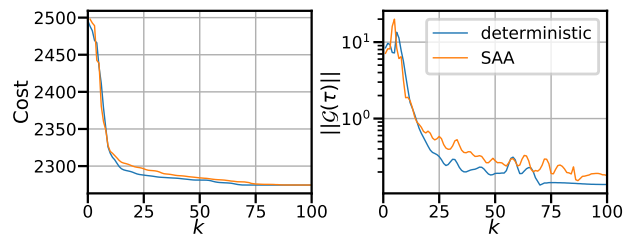


Figure 14: Convergence of BFGS method to the deterministic optimal solution in Fig. 9 (in blue) and to the SAA-based optimal solution in Fig. 12 (in orange). (left) Cost value versus iteration number. (right) Gradient norm versus iteration number.

(a) $\delta = 25, \gamma = 2.5$

	x	y	maximum amplitude
mean (deterministic)	9.61	6.01	20.93
variance (deterministic)	0.0083	0.0015	0.112
mean (SAA)	9.59	5.99	21.76
variance (SAA)	0.0023	0.00015	0.078

(b) $\delta = 12.5, \gamma = 1.25$

	x	y	maximum amplitude
mean (deterministic)	9.6	6.02	19.4
variance (deterministic)	0.02	0.005	1.27
mean (SAA)	9.61	6.01	21.76
variance (SAA)	0.008	0.0017	0.33

Table 1: Mean and variance values of PNJ properties: location (x, y) and maximum amplitude, resulting from noise polluted lenses. (Table (a), first and second rows) the statistics are computed from the optimal lens in the deterministic case, Fig. 9a, by polluting it by 15 different manufacturing error realizations. (Table (a), third and fourth rows) the statistics are computed from the optimal lens in the SAA OUU case, Fig. 12a, by polluting it by the same 15 manufacturing error realizations. For both cases summarized in Table (a), $\delta = 25$ and $\gamma = 2.5$. Table (b) reports the statistics of a similar study that differs only in the manufacturing error model where $\delta = 12.5$ and $\gamma = 1.25$, leading to a doubled error level compared to the case in Table (a).

4 Conclusion

In this work, we demonstrate that designing PNJs through an optimized heterogeneous lens profile design is computationally feasible and provides flexibility in designing the location of the desired PNJ. Additionally, incorporating manufacturing uncertainty in the optimization problem of the heterogeneous lens design gives a non-trivial optimal lens design that achieves robust PNJ design. Some future work will be on alternative stochastic formulation using probability or chance constraint Chen and Ghattas [2021] to control the defect rate, optimal design with design constraint to facilitate more feasible manufacturing, and experimental validation of the proposed computational results.

Acknowledgments

Karamehmedović and Alghamdi were supported by The Villum Foundation (grant no. 25893). Karamehmedović also received funding within the project (20FUN02/f10 POLight) from the EMPIR programme cofinanced by the Participating States and by the European Union’s Horizon 2020 research and innovation programme. Chen was partially supported by NSF DMS grant 2012453, USA.

Appendix: Matern Covariance

We assume $\zeta \sim \mathcal{N}(0, \mathcal{C})$ where $\mathcal{N}(0, \mathcal{C})$ is a Matérn class infinite dimensional Gaussian random field with zero mean and covariance operator \mathcal{C} . To sample from $\mathcal{N}(0, \mathcal{C})$ efficiently, we employ the link between Matérn class Gaussian random fields and elliptic Stochastic Partial Differential Equations (SPDE) Lindgren et al. [2010], Villa et al. [2021].

$$\begin{aligned} (\delta I - \gamma \Delta)^{\alpha/2} \zeta(x) &= w(x) \quad \text{in } \mathcal{D} \\ \nabla \zeta \cdot n &= 0 \quad \text{on } \delta \mathcal{D}, \end{aligned}$$

where $w(x)$ is white noise. The choice of δ and γ dictates the variance and the correlation length of the Gaussian field spacial features. α is a smoothing parameter that satisfies $\alpha > d/2$ for variance boundedness. For the choice of $\alpha = 2$, generating a sample from this field, amounts to solving the elliptic system above, with a white noise sample $w(x)$ as the right-hand side, and a matrix-vector product Lindgren et al. [2010]. Solving this system can be done scalably using multigrid method Villa et al. [2021].

References

- Zhigang Chen, Allen Taflove, and Vadim Backman. Photonic nanojet enhancement of backscattering of light by nanoparticles: a potential novel visible-light ultramicroscopy technique. *Opt. Express*, 12(7):1214–1220, Apr 2004. doi:10.1364/OPEX.12.001214. URL <http://opg.optica.org/oe/abstract.cfm?URI=oe-12-7-1214>.
- X. Li, Z. Chen, A. Taflove, and V. Backman. Optical analysis of nanoparticles via enhanced backscattering facilitated by 3-d photonic nanojets. *Opt. Express*, 13:526–533, 2005.
- Arash Darafshah. Photonic nanojets and their applications. *Journal of Physics: Photonics*, 3(2):022001, 2021.
- Mirza Karamehmedović, Kenneth Scheel, Frederik Listov-Saabye Pedersen, and Poul-Erik Hansen. Imaging with a steerable photonic nanojet probe. submitted, 2022a.
- S. Lecler, S. Perrin, A. Leong-Hoi, and P. Montgomery. Photonic jet lens. *Sci. Rep.*, 9:4725, 2019.
- J. Zhu and L. L. Goddard. Spatial control of photonic nanojets. *Opt. Express*, 24:30444, 2016.
- A. Paganini, S. Sargheini, R. Hiptmair, and C. Hafner. Shape optimization of microlenses. 23:13099, 2015.
- Yajie Chen, Ying Wang, Xintao Zeng, Shifa Pan, Musheng Chen, Yongxi Zeng, Baoyu Fu, Pinghui Wu, and Miao Pan. Ultrahigh quality factor photonic nanojets generated by truncated microtoroid structures. *IEEE Photonics Journal*, 13(4):1–6, 2021a. doi:10.1109/JPHOT.2021.3100136.
- Zhu Hengyu, Chen Zaichun, Chong Tow Chong, and Hong Minghui. Photonic jet with ultralong working distance by hemispheric shell. *Opt. Express*, 23(5):6626–6633, Mar 2015. doi:10.1364/OE.23.006626. URL <http://opg.optica.org/oe/abstract.cfm?URI=oe-23-5-6626>.
- Yuri E. Geints, Alexander A. Zemlyanov, and Ekaterina K. Panina. Photonic nanojet calculations in layered radially inhomogeneous micrometer-sized spherical particles. *J. Opt. Soc. Am. B*, 28(8):1825–1830, Aug 2011. doi:10.1364/JOSAB.28.001825. URL <http://opg.optica.org/josab/abstract.cfm?URI=josab-28-8-1825>.
- Mirza Karamehmedović, Kenneth Scheel, Frederik Listov-Saabye Pedersen, Arturo Villegas, and Poul-Erik Hansen. Steerable photonic jet for super-resolution microscopy. submitted, 2022b.
- Eli Turkel and A Yefet. Absorbing PML boundary layers for wave-like equations. *Applied Numerical Mathematics*, 27(4):533–557, 1998.
- Finn Lindgren, Johan Lindström, and Håvard Rue. An explicit link between gaussian fields and gaussian markov random fields; the spde approach. 2010.
- Peng Chen, Michael R Haberman, and Omar Ghattas. Optimal design of acoustic metamaterial cloaks under uncertainty. *Journal of Computational Physics*, 431:110114, 2021b.
- Max D Gunzburger. *Perspectives in flow control and optimization*. SIAM, 2002.
- Peng Chen. Stochastic optimization under high-dimensional uncertainty in python (soupy). <https://github.com/cpempire/soupy>, 2021.
- Richard H Byrd, Peihuang Lu, Jorge Nocedal, and Ciyou Zhu. A limited memory algorithm for bound constrained optimization. *SIAM Journal on scientific computing*, 16(5):1190–1208, 1995.
- Peng Chen and Omar Ghattas. Taylor approximation for chance constrained optimization problems governed by partial differential equations with high-dimensional random parameters. *SIAM/ASA Journal on Uncertainty Quantification*, 9(4):1381–1410, 2021.
- Umberto Villa, Noemi Petra, and Omar Ghattas. HIPPylib: An Extensible Software Framework for Large-Scale Inverse Problems Governed by PDEs: Part I: Deterministic Inversion and Linearized Bayesian Inference. *ACM Trans. Math. Softw.*, 47(2), April 2021. ISSN 0098-3500. doi:10.1145/3428447. URL <https://doi.org/10.1145/3428447>.